Materials Advances

ROYAL SOCIETY OF CHEMISTRY

PAPER

View Article Online
View Journal | View Issue



Cite this: *Mater. Adv.*, 2026, 7, 5791

# Waste-to-work photocatalysis: orange-peel-derived CQD@CdS/biochar hybrids enabling efficient visible-light-driven dye mineralisation and mechanistic elucidation

Akash M. Nair,†[a] Palkaran Sethi,†[b] Jasminder Singh*[a] and Soumen Basu *[b]

The uncontrolled discharge of organic dyes into aquatic systems necessitates the development of efficient and sustainable photocatalysts for environmental remediation. In this work, a green and resource-efficient strategy was employed to synthesize a CQD@CdS/biochar nanocomposite using orange peel waste as a renewable carbon precursor and aloe vera extract as a natural reaction medium. Structural and physicochemical characterization using XRD, FTIR, XPS, FESEM, UV–Vis DRS, PL, and BET confirmed the successful formation of the composite. The photocatalytic activity was evaluated through the degradation of methylene blue under visible-light irradiation. Among the prepared samples, the optimized 5% CQD@CdS/biochar (5CC) composite exhibited superior performance, achieving 96.2% dye removal within 120 min and following pseudo-first-order kinetics with a rate constant of 0.0061 $min^{-1}$, outperforming the pristine materials and $TiO_2$-P25. The catalyst also demonstrated good stability, retaining 89.6% of its activity after five reuse cycles. Radical trapping experiments revealed •OH radicals as the dominant reactive species responsible for degradation. Furthermore, significant mineralization was confirmed by COD and TOC reductions of 63% and 66%, respectively, supported by HRMS identification of degradation intermediates and a proposed reaction pathway. These findings highlight the potential of waste-derived CQD@CdS/biochar as an efficient photocatalyst for visible-light-driven wastewater treatment.

Received 9th January 2026,
Accepted 2nd May 2026

DOI: 10.1039/d6ma00043f

rsc.li/materials-advances



## 1. Introduction

Water pollution from synthetic dyes has become a pressing environmental concern due to the uncontrolled discharge of dye-laden wastewater from industries such as textiles, paper, and leather.[1] Over 10 000 dyes are commercially produced, with around 700 000 tons manufactured annually, and 10–15% of these entering water bodies during production and dyeing.[2] Many dyes are non-biodegradable, toxic, and resistant to light, temperature, and microbial attack, causing long-term contamination of aquatic ecosystems.[3] Beyond aesthetic concerns, these dyes pose serious risks: they can be carcinogenic, mutagenic, or allergenic, reduce dissolved oxygen, and block sunlight penetration, thereby disrupting photosynthesis in aquatic organisms.[4]

Methylene blue (MB), a commonly used synthetic dye, exemplifies these hazards.[5] Its persistence in water reduces light availability for aquatic plants, bioaccumulates in organisms, and induces oxidative stress through the generation of reactive oxygen species (ROS), which subsequently induce lipid peroxidation, genetic material impairment, and cellular dysfunction.[6] Human exposure to MB-contaminated water may cause methemoglobinemia in infants,[7] gastrointestinal irritation, dizziness, nausea, and potential neurotoxicity,[8] highlighting the need for effective removal strategies.[9,10]

Conventional remediation methods such as adsorption,[11] coagulation–flocculation, and nanofiltration have been widely employed. Adsorption using activated carbon effectively concentrates dyes on solid surfaces but merely transfers contaminants without eliminating them, necessitating regeneration or disposal of spent adsorbents.[12] Coagulation–flocculation aggregates dye colloids into flocs, which can be separated, but generates chemical sludge and may leave residual dissolved dyes.[13,14] Nanofiltration (NF) can remove >90% of dye content but suffers from high operating pressure, membrane fouling, and high costs.[15,16] These limitations underscore the need for more sustainable and efficient water treatment technologies.

[a] *Department of Chemistry, School of Chemical Engineering and Physical Sciences, Lovely Professional University, Phagwara, Punjab 144411, India. E-mail: jasminder.singh91@gmail.com*
[b] *Department of Chemistry and Biochemistry, Thapar Institute of Engineering & Technology, Patiala-147004, India. E-mail: soumen.basu@thapar.edu*
† Both authors have equal contribution.

Photocatalysis has emerged as a promising alternative, operating under ambient conditions using light energy, without producing harmful sludge or secondary pollutants. Conventional photocatalysts like $TiO_2$ and ZnO work under UV light, while visible-light-responsive semiconductors such as graphitic carbon nitride and cadmium sulfide have gained attention for practical solar-driven applications.[11,17,18] CdS, with a narrow band gap ($\sim$2.4 eV), efficiently absorbs visible light and its photo-response can be tuned by size or composition.[19] Coupling CdS with other materials or forming heterojunctions enhances charge separation, broadens light absorption, and improves stability and quantum efficiency.[16] For instance, CdS/g-$C_3N_4$ composites have shown several-fold higher dye degradation than individual components.[20] The advantages of complete mineralization, absence of secondary waste, utilization of renewable light energy, and the design of tunable, efficient catalysts collectively position photocatalysis as a sustainable and promising strategy for wastewater remediation.[21]

Carbon-based materials further improve photocatalytic performance by acting as co-adsorbents and electron sinks. They provide high surface area to concentrate dye molecules and facilitate charge separation.[22] Previous studies, such as $Bi_2O_3$/Ag/graphene[23] and ZnO–Ag/graphene[24] composites, demonstrated superior dye removal and photodegradation compared to bare semiconductors. Despite these advances, combining CdS with biomass-derived carbon supports remains underexplored. Notably, biochar, a cost-effective porous carbon derived from biomass, and green-synthesized carbon quantum dots (CQD) have yet to be systematically investigated as co-catalysts in CdS-based systems.

In the present study, a CQD@CdS/Biochar composite photocatalyst was developed using varying weight ratios *via* a green synthesis method, employing orange peel powder as a renewable carbon source and aloe vera solvent system for CdS. The resulting hybrid leverages the synergistic roles of CQD as photosensitizers and electron mediators and biochar as a conductive support, enabling efficient methylene blue (MB) degradation under visible light. Comprehensive characterisation (XRD, FTIR, XPS, FESEM, UV–Vis DRS, PL, BET) validated the successful formation and coupling of the composite. Photocatalytic efficiency was evaluated through parameter optimisation, active species trapping, and HRMS-based degradation pathway studies, while TOC/COD analyses confirmed the material's strong mineralisation potential. The excellent cyclic stability and retention of crystal structure after photocatalytic use, as evidenced by XRD, highlight the durability of the green-synthesized hybrid and its promise as an environmentally benign photocatalyst for long-term wastewater remediation.

# 2. Experimental details

## 2.1. Chemicals and raw materials

The materials were synthesised using cadmium carbonate ($CdCO_3$) and sodium sulfide ($Na_2S$), purchased from Loba Chemie, and are of extra-pure quality. The CQD and biochar were synthesised using orange peel powder obtained from the local fruit market. The green solvent was synthesised from aloe vera gel, which was obtained from the agricultural fields of Thapar Institute of Engineering and Technology. Methylene blue (MB) powder was procured from Loba Chemie, and all solutions were prepared using ultrapure double-distilled water. All reagents utilized in this study were of analytical grade and employed directly without any additional purification.

## 2.2. Synthesis of ternary composites

**2.2.1. Synthesis of biochar from orange peels.** The biochar is synthesised *via* a hydrothermal method using a Teflon-lined autoclave. The orange peels are dried under the sun for 2 days and then powdered using a blender. The fine powder is used for the synthesis of biochar. 10 g of the powder is then transferred into a 150 mL autoclave along with 60 mL of deionised water. The pH of the mixture is then set around 3–4 using 0.1 N HCl. This dispersed mixture is then transferred into a controlled muffle furnace for hydrothermal carbonisation treatment at 210 °C for 3 h with a rate of heating of 3 °C $min^{-1}$. Let the mixture cool at room temperature, followed by filtering, washing and then drying the obtained biochar at 90 °C overnight and labelled as BC.[25]

**2.2.2. Synthesis of CQD.** The orange peel powder obtained is used for the synthesis of CQD *via* the hydrothermal method. 5 g of the powder is subsequently placed into a 150 mL Teflon-lined stainless-steel autoclave with 50 mL of deionised water. The autoclave is then transferred into a controlled muffle furnace for hydrothermal treatment at 200 °C for 12 h. After completion of the reaction, the system was allowed to cool naturally to ambient temperature, followed by filtration to obtain the CQD solution.[26]

**2.2.3. Synthesis of CdS.** For the synthesis of CdS, fresh Aloe vera gel was collected by scooping it out from the inner portion of the leaves and heating it in 400 mL of distilled water until the volume was reduced to 80 mL to concentrate the bioactive constituents. The concentrated extract was filtered through Whatman filter paper to obtain a clear green solvent, which served as both the reaction medium and a natural reducing, capping, and stabilizing agent, owing to its abundant polyphenols, flavonoids, amino acids, and vitamins that regulate nanoparticle nucleation and suppress aggregation. For CdS formation, cadmium acetate (1 M) and sodium sulfide (1 M) were each dissolved in 20 mL of the Aloe vera extract and mixed slowly under constant stirring to avoid abrupt precipitation. The reaction mixture was continuously stirred for 3 h at room temperature. The resulting yellow precipitate was separated *via* centrifugation and thoroughly washed several times with distilled water and ethanol to eliminate residual impurities and unreacted precursors. The purified product was then dried at 60 °C for 6 h to obtain pure CdS.[27]

**2.2.4. Synthesis of CQD@CdS/biochar nanocomposites.** The synthesis of the composite was done *via* an *in situ* method. The CdS precursors were prepared using a green solvent synthesised from aloe vera extract, which also acts as a capping agent for the nanoparticle synthesis. The precursors are prepared

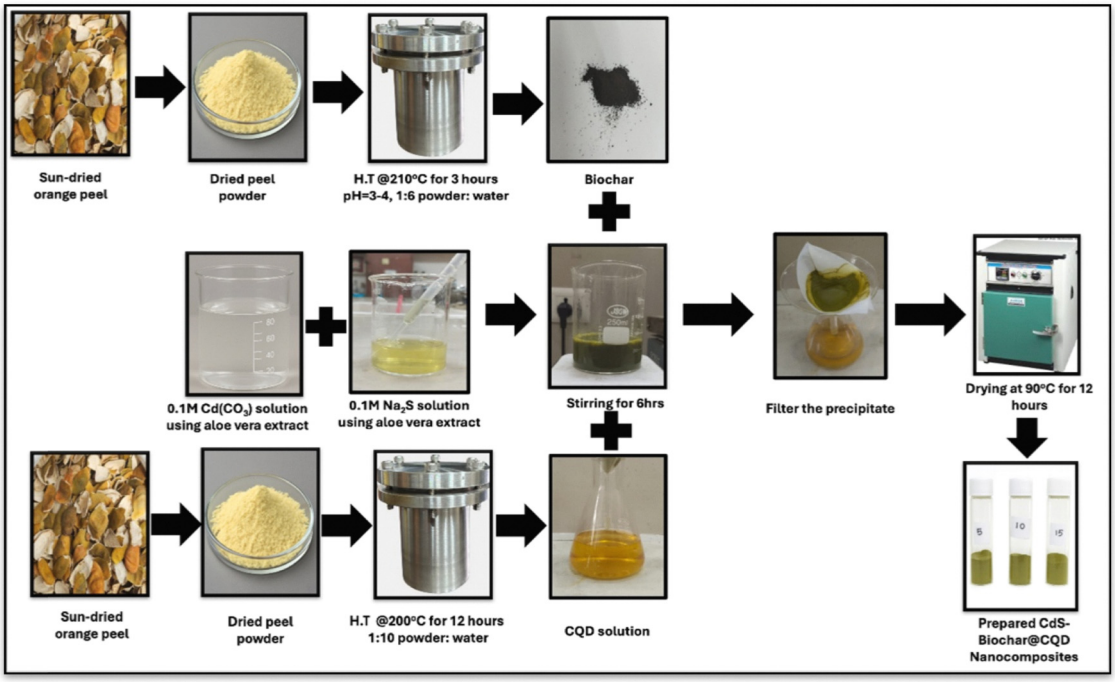


Scheme 1 Schematic representation of the synthesis route for CQD@CdS/biochar nanocomposites.

with a concentration of 0.1 M. The precursors, along with the BC prepared, are then transferred into a beaker with a 2 : 3 w/w ratio. The synthesised CQD solution is also transferred into the mixture according to the weight % (5,10 and 15). The mixture is then stirred while maintaining a temperature of 30–40 °C for 6 hours. The resulting mixture was subsequently filtered and dried in a hot-air oven at 90 °C for 12 h to ensure complete removal of moisture. The samples were then labelled 5CC,10CC and 15CC according to the weight % of CQD present in the composite (Scheme 1).

For comparison, a binary CdS/BC composite without CQD was also prepared using the same procedure. CdS precursors and biochar (BC) were mixed in a 2 : 3 (w/w) ratio, stirred at 30–40 °C for 6 h, filtered, and dried at 90 °C. This sample, lacking CQDs, served to examine the effect of CQD incorporation on photocatalytic activity. This binary composite was labelled CBc for clarity.

**2.2.5. Photocatalysis experiments.** The photocatalytic degradation of methylene blue (MB) was systematically studied through a detailed experimental procedure. A concentrated 100 ppm MB stock solution was prepared by dissolving 2.5 mg of MB in 25 mL of deionized water. This solution was then diluted to a 10 ppm working concentration. A volume of 10 mL of the 10 ppm solution was mixed with varying catalyst doses (ranging from 0.1 to 1.2 g $L^{-1}$) and stirred for 20 to 120 minutes in the dark to allow for adsorption equilibrium. The mixtures were then exposed to light in order to optimize the degradation process. The pH of the MB solutions was adjusted across a range from 1 to 12 using HCl or NaOH, and pH levels were monitored with a pH meter. After degradation, the catalyst was separated by centrifugation at 6000 rpm, and the remaining MB concentration in the supernatant was measured at 658 nm using a UV-Vis spectrophotometer to assess adsorption and degradation efficiency (eqn (1)). Each experiment was repeated three times, with error bars showing a 5% margin of error, ensuring accurate optimization of conditions for effective MB removal. This thorough approach ensured precise optimization of the conditions for effective MB removal.

$$\text{Degradation}\,(\%) = \frac{C_0 - C_t}{C_t} \times 100 \qquad (1)$$

where $C_0$ and $C_t$ are the before and after degradation concentrations of methylene blue.

**2.2.6. Characterisation.** Comprehensive characterisation details confirming the structural, surface, and morphological features of the synthesised composites are provided in Section S1 in SI.

# 3. Results and discussions

## 3.1. Characterisations

**3.1.1. XRD analysis.** The XRD patterns of CdS, CQD, BC, CBc, 5CC, 10CC, and 15CC are shown in Fig. 1(a). Distinct diffraction peaks at $2\theta \approx 24.8^\circ$, $26.5^\circ$, $28.2^\circ$, $43.7^\circ$, $47.8^\circ$, and $51.8^\circ$ correspond to the (100), (002), (101), (110), (103), and (112) planes of hexagonal CdS (JCPDS No. 77-2306),[28] confirming its crystalline wurtzite phase. BC exhibits broad humps around $23^\circ$ and $44^\circ$, corresponding to the (002) and (100) planes of turbostratic carbon, indicating its amorphous nature.[29] CQD display a broad reflection near $22^\circ$, attributed to disordered graphitic carbon domains.[30] When CQD are incorporated into the composite, they cause a noticeable shift

in the XRD peaks. Specifically, the diffraction peaks of CdS in CBc and ternary composites (5CC, 10CC, 15CC) exhibit slight broadening and a marginal shift toward lower angles. This suggests that the integration of CQD into the composite



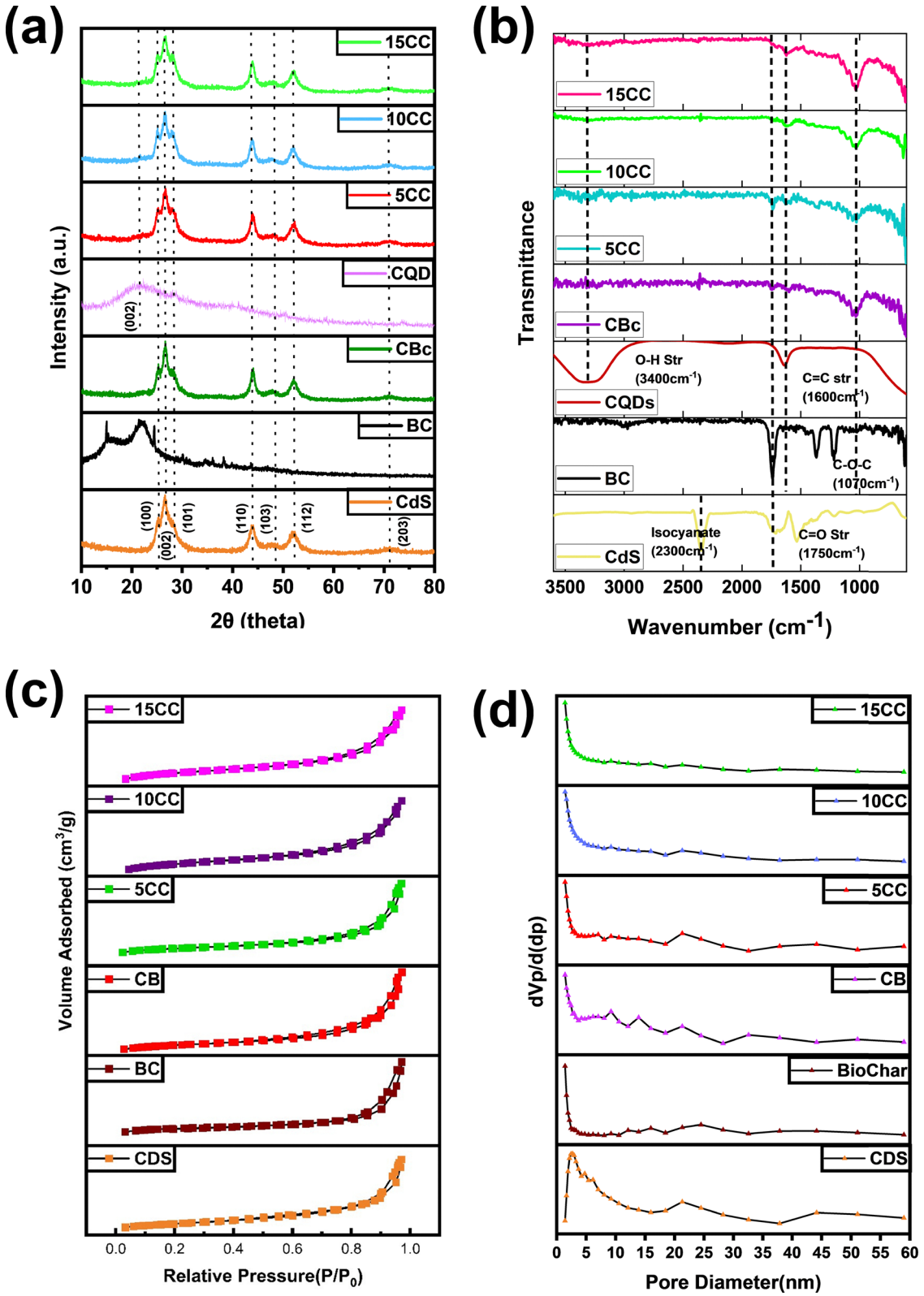


Fig. 1 (a) XRD pattern, (b) FTIR spectra, (c) adsorption and desorption isothermsand (d) pore size distribution for different materials (CdS, BC, CBc, 5CC, 10CC, and 15CC).

enhances the structural interfacial interaction and lattice distortion. The CQD incorporation helps to promote better coupling between CdS and the BC matrix, potentially facilitating charge transfer and improving the overall stability and functionality of the composite material. For CBc and the ternary composites (5CC, 10CC, 15CC), the major CdS peaks are retained with slight peak broadening and marginal shifts toward lower angles, suggesting lattice distortion and strong interfacial interaction among the components. No additional impurity peaks are detected, confirming high phase purity. These observations indicate that CdS nanoparticles are uniformly embedded within the BC matrix, while CQD incorporation enhances structural integration and interfacial coupling, confirming the successful formation of the ternary nanocomposite.

**3.1.2. FT-IR measurement.** FTIR spectra were employed to verify the surface functionalities and interfacial interactions in CdS, BC, CQD, the binary CBc, and the ternary composites (Fig. 1(b)). The green-synthesized CdS (using *Aloe vera* gel extract) showed a characteristic Cd–S stretching band in the 610–670 $cm^{-1}$ region, along with additional bands attributable to biomolecular residues from the extract. The peaks at ~1700–1720 $cm^{-1}$ and 1100–1200 $cm^{-1}$ reflect C═O and C–O/C–O–C vibrations, respectively, likely originating from polysaccharides, phenolics, and proteins present in the aloe extract that acted as capping and stabilizing agents.[31,32] BC displayed its characteristic O–H (~3400 $cm^{-1}$), aliphatic C–H (2920–2850 $cm^{-1}$), and aromatic C═C/C═O bands (~1620 $cm^{-1}$), consistent with lignocellulosic char materials.[33] CQD exhibited abundant oxygenated groups with clear O–H, C═O, and C–O vibrations, confirming their surface passivation.[34] In the binary CBc and ternary composites (5CC, 10CC, 15CC), overlapping features from CdS, BC, and CQD were observed. Notably, the O–H and C═O peaks broadened and shifted slightly, indicating hydrogen bonding and electrostatic interactions between CdS (aloe-derived surface groups), BC, and CQD. Such interfacial interactions play a crucial role in enhancing photocatalytic activity by facilitating charge separation, reducing recombination, and enabling more efficient electron transfer across the heterostructure.[35]

**3.1.3. BET surface area analysis.** The specific surface area (BET analysis), pore size distribution, and overall pore volume of CdS, BC, binary composite CBc, and ternary composites 5CC, 10CC, and 15CC were assessed using $N_2$ adsorption isotherms, as shown in Fig. 1(c) and Table 1. $N_2$ adsorption–desorption isotherms of all the pristine materials and the composites exhibit type IV adsorption isotherms, with H3-type hysteresis loops, which are similar to mesoporous materials with slit-shaped pores, ascribed to the carbonaceous framework. The isotherms exhibit enhanced nitrogen adsorption at high relative pressures ($P/P_0 > 0.8$), owing to capillary condensation occurring within the mesoporous channels. The surface area and pore volume of 5CC, were higher than the other composite samples, 10CC and 15CC. BJH pore size distribution analysis also corroborates the mesoporous characteristic of the samples (Fig. 1(d)), and the average pore size is about 9–17 nm. Incorporating 5–15% CQD lightly modified the pore structure and narrowed the pore size distribution. Among the composites, the 5CC sample exhibited a comparatively more uniform pore structure, which may facilitate effective interaction between the catalyst surface and dye molecules during the photocatalytic process.

Table 1 BET surface area, cumulative pore volume, and mean pore diameter

| Sample | Pore nm) | Surface area ($m^2\ g^{-1}$) | Total pore volume ($cm^3\ g^{-1}$) |
|---|---|---|---|
| CdS | 11.886 | 51.631 | 0.1406 |
| BC | 16.969 | 5.73 | 0.0182 |
| CBc | 13.532 | 19.221 | 0.0572 |
| 5CC | 15.565 | 15.875 | 0.0448 |
| 10CC | 9.8814 | 13.584 | 0.0257 |
| 15CC | 9.2051 | 13.966 | 0.0249 |

**3.1.4. XPS analysis.** The XPS spectra of the 5CC nanocomposite (Fig. 2) verify the presence of C, O, N, Cd, and S elements, indicating successful composite formation with distinct chemical states. The C 1s spectrum displays three characteristic peaks at 284.6 eV (C–C/C═C), 285.9 eV (C–O/C–N), and 288.6 eV (O–C═O), corresponding to the carbon backbone and surface functional moieties of CQD. The O 1s spectrum shows signals assigned to lattice oxygen (~529.8 eV), oxygen vacancies (~531.4 eV), and hydroxyl or adsorbed oxygen (~532.6 eV), highlighting the presence of oxygen-enriched sites and structural defects. The N 1s signal at approximately 404 eV is associated with oxidized nitrogen species ($NO_2$ or $NO_3^-$), originating from nitrogen–oxygen surface interactions or partial oxidation of CQD. The Cd 3d doublet with peaks at 405.1 and 411.8 eV is characteristic of $Cd^{2+}$ in CdS, while the S 2p peaks at 160.3 and 161.7 eV correspond to $S^{2-}$ species in Cd–S bonds without any detectable oxidation.[36]

Overall, the XPS analysis substantiates the successful synthesis and elemental integration within the 5CC composite with stable Cd–S bonding, N/O functionalization, and defect states that promote efficient interfacial charge transfer and enhanced photocatalytic activity.

**3.1.6. FESEM-EDS mapping.** The surface morphology of the synthesised samples was studies using FESEM studies and illustrated in Fig. 3(a)–(c). FESEM is a powerful tool for analysing the surface morphology and structural properties of CdS, BC and 5CC nanocomposite. The CdS FESEM images gave a nano-globular structure within a 100 nm scale.[37] For the FESEM images of the hydrothermally synthesised BC, the surface comprises a porous structure that can aid in the impressive adsorption of the dye.[22] It can also be decorated with CdS nanoglobules coated with CQD. The 5CC nanocomposite has a heterogeneous surface structure due to the integration of CdS into the BC matrix along with the desired percentage of CQD (5%). The surface at a 500 nm scale study shows the nanoglobules coated on the surface of the porous BC.

The elemental composition of the synthesized 5CC nanocomposite was determined using energy-dispersive X-ray spectroscopy (EDS) and corresponding color mapping in Fig. 3(d), which revealed a uniform elemental distribution, indicating that Cd, S, C, O, and N are homogeneously dispersed across the composite

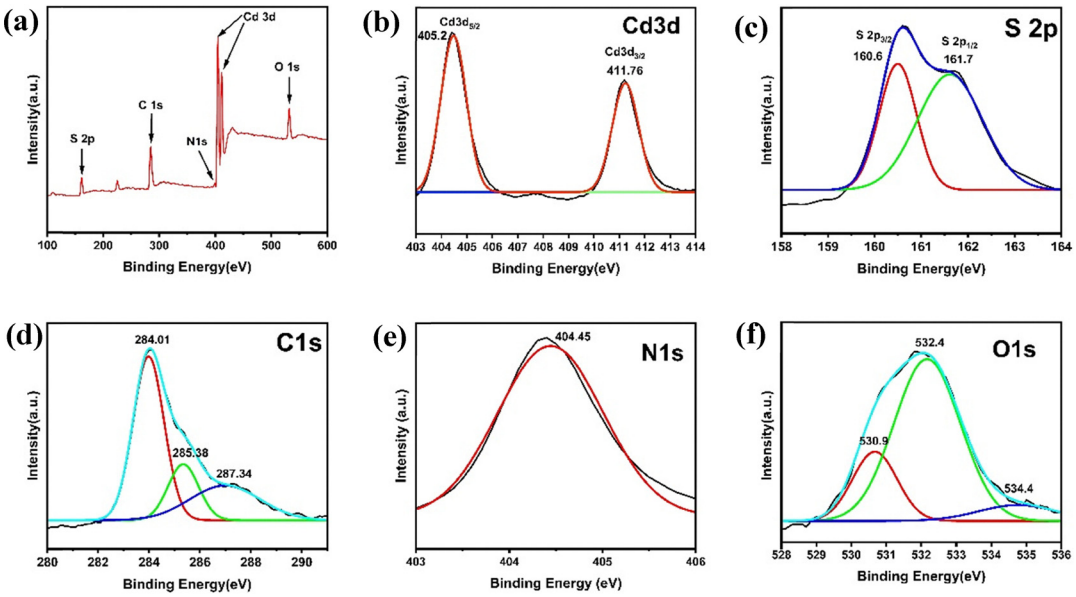


Fig. 2 (a) XPS survey spectrum of 5CC, and high-resolution spectra of (b) Cd 3d, (c) S 2p, (d) O 1s, (e) N 1s, and (f) C 1s core levels.

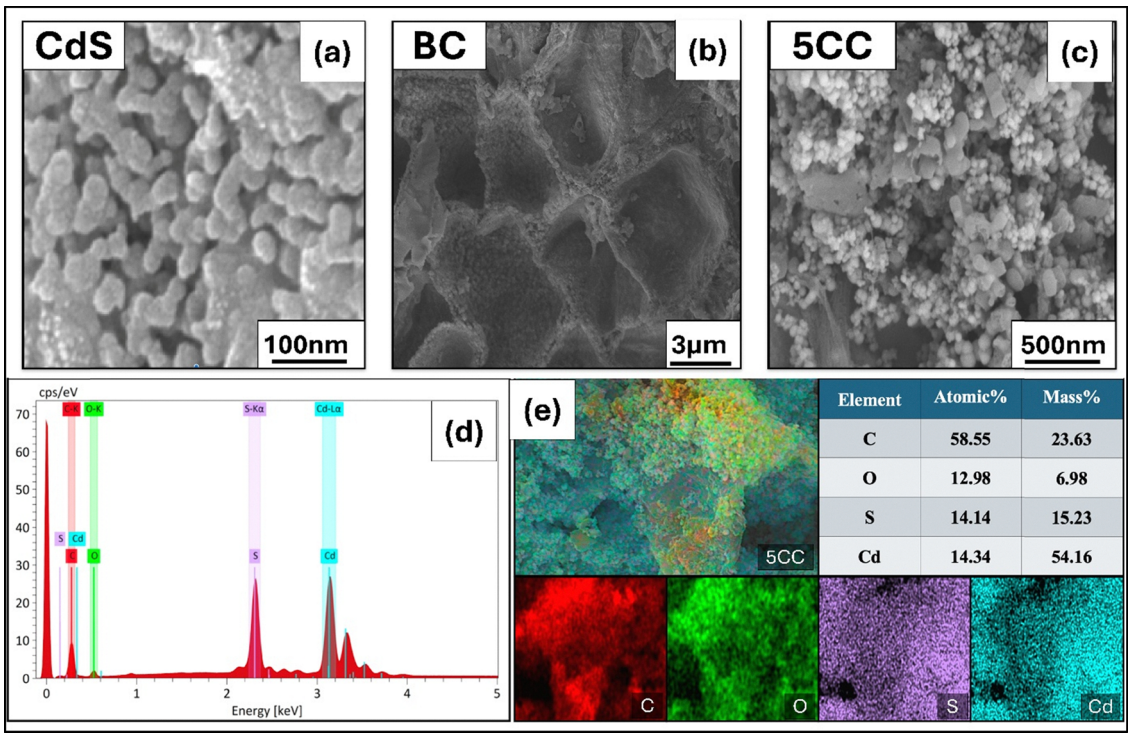


Fig. 3 FE-SEM micrographs of (a) CdS, (b) BC, (c) 5CC, (d) EDS analysis, and (e) colour mapping of different elements of 5CC.

surface. The EDS spectrum distinctly displayed the presence of Cd, S, C, and O elements. The weight composition of the 5CC nanocomposite was determined to be 54.16% Cd, 15.23% S, 23.63% C, and 6.98% O. In terms of atomic percentages, Cd and S accounted for 14.34% and 14.14%, respectively, while C and O—originating from BC and the CQD solution—comprised 58.55% and 12.98%, respectively.

**3.1.7. Photoluminescence characterization.** The photoluminescence (PL) spectra of all the pristine materials and the nanocomposites with different CQD loadings of 5%, 10%, and 15% show significant differences in PL intensity, providing crucial insights into the charge recombination process (Fig. 4(a)). Its emission peak at 705 nm is attributed to the recombination of electron/hole pairs in the CdS. The emission

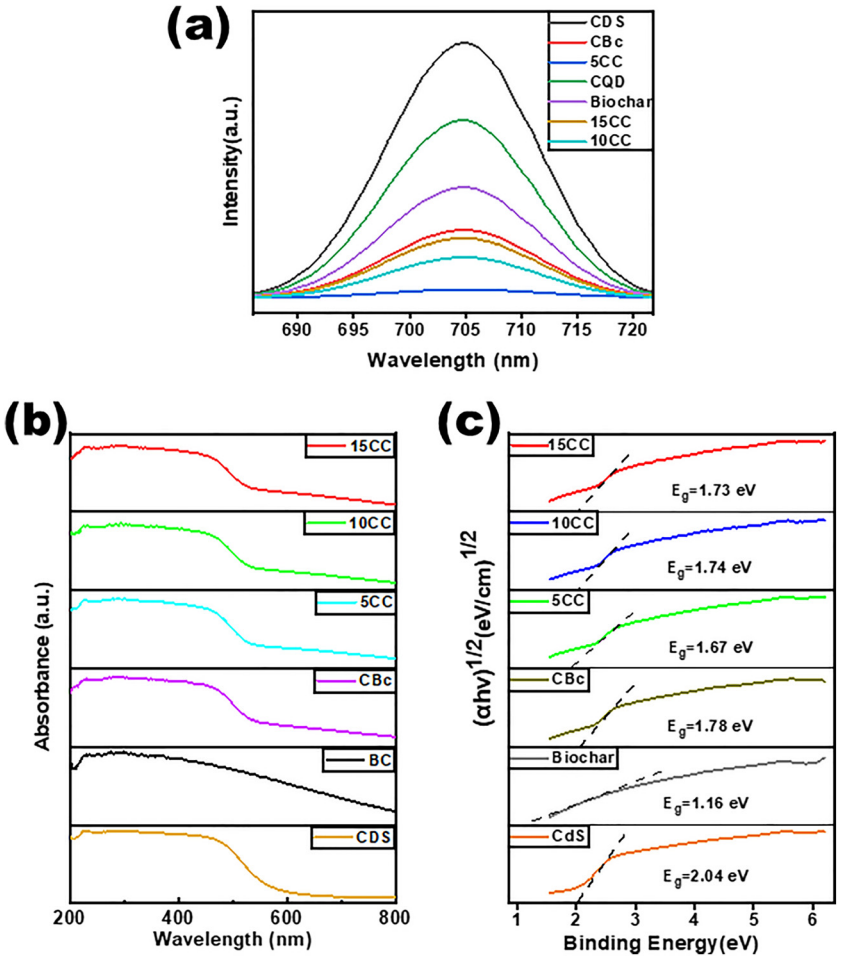


Fig. 4 (a) PL spectra of various catalysts (CdS, CBc, 5CC, 10CC, CQD, BC,15CC), revealing their potential in photocatalytic applications, (b) UV-vis DRS spectra, (c) Tauc plot of 5CC, 10CC,15CC, CBc, BC and CdS.

band at 705 nm results from electron–hole pair recombination within the CdS lattice. As the CQD content varies from the binary CBc to the ternary composites (5CC, 10CC, and 15CC), the PL emission intensity gradually decreases, indicating enhanced charge separation. 5CC, with 5% CQD loading, exhibits the weakest PL intensity, suggesting that incorporating CQD promotes effective separation of the CdS/BC and CQD, reducing electron–hole recombination, and leading to the highest photocatalytic activity. However, PL intensity increases somewhat in 10CC and 15CC with higher CQD loadings, implying that excess CQD may cause aggregation, thus decreasing charge separation efficiency. This trend aligns with previous studies showing that, although CQD can enhance charge separation by acting as electron sinks, an excessive amount of CQD may impair electron mobility, ultimately reducing overall photocatalytic performance.[38] Therefore, PL analysis confirms that 5CC, with an optimal CQD amount, exhibits the highest photocatalytic efficiency, making it the most effective composite for degrading methylene blue.

**3.1.8. UV-Vis DRS and Mott Schottky analysis.** The optical absorption characteristics and band gap energies of the synthesized materials were examined using Diffuse Reflectance Spectroscopy (DRS). Fig. 4(b) illustrates that the photocatalysts demonstrate significant absorption within the visible-light region. The corresponding band gap values were determined from the Tauc plot shown in Fig. 4(c), based on eqn (2).

$$(\alpha h\nu)^{1/2} = h\nu - E_g \quad (2)$$

In this expression, the variables $h$, $\nu$, $\alpha$, and $E_g$ represent Planck's constant, light frequency, absorption coefficient, and band gap energy, respectively. The band gap energy was estimated from the intercept of the linear region of the Tauc plot with the $x$-axis.[39] The calculated band gaps of CdS, BC, Binary composite (CBc), and their composites (5,10,15) CC were 2.04, 1.169, 1.78, 1.67, 1.74 and 1.73 eV, respectively. From these studies, it was evident that the 5CC sample had the lowest energy after the BC, which is photocatalytically inactive. The decrease in the nanocomposites' bandgap from the bare materials can improve the photocatalytic efficiency of the sample. To further verify the electronic band structure of the materials, Mott–Schottky (M–S) measurements were carried out using a three-electrode electrochemical system. The Mott–Schottky plots (Fig. S1 in SI) exhibited positive slopes for all samples, confirming their n-type semiconductor nature.[40] The flat band potentials were determined from the intercepts of the linear regions and were found to be approximately −0.61 V for BC,

−0.89 V for CdS, and −0.988 V for CQD *versus* Ag/AgCl. For n-type semiconductors, the flat band potential is generally considered to be close to the conduction band potential; therefore, the conduction band positions of BC, CdS, and CQD were estimated to be near these values. Using the band gap values obtained from DRS analysis, the corresponding valence band potentials were subsequently estimated, indicating favorable band alignment that can promote efficient charge separation and facilitate electron transfer during the photocatalytic process.

**3.1.9. Characterisations of CQD.** The synthesized CQD were characterized to examine their morphology, particle size distribution, and optical properties using HRTEM, UV–Vis spectroscopy, and fluorescence spectroscopy (Fig. S2 in SI). The morphology and size of the synthesized CQD were investigated using high-resolution transmission electron microscopy (HRTEM). As shown in Fig. S2(a), the CQD are well dispersed and exhibit a nearly spherical morphology. The particle size distribution calculated from the HRTEM images (Fig. S2(b)) indicates that the CQD possess nanoscale dimensions with a relatively narrow size distribution with average size of 3.4 nm. The optical properties of the CQD were further examined using UV–Vis absorption and fluorescence spectroscopy. The UV–Vis spectrum (Fig. S2(c)) shows characteristic absorption features associated with the π–π* transitions of C=C bonds. Additionally, the fluorescence emission spectrum (Fig. S2(d)) exhibits strong photoluminescence behavior, which is a typical characteristic of CQD. These results confirm the successful formation of CQD with well-defined nanoscale morphology and optical properties.

### 3.2. Impact of the catalyst dose

The amount of catalyst utilised has the greatest impact on the photocatalyst's efficiency. To investigate how dosage affects MB degradation, studies were carried out with varied doses of the 5CC from 1 to 12 mg, while the MB concentration remained constant at 10 ppm for 120 min in light (Fig. 5(a)). At the lowest dosage (0.1 g $L^{-1}$), MB breakdown involved fewer active species, resulting in lower photocatalytic effectiveness. Optimal degradation efficiency was achieved at 0.6 g $L^{-1}$ maximizing the availability of active sites and the utilization of light energy, after which the efficiency reached a plateau. Further increasing the catalyst dosage beyond 0.2 g $L^{-1}$ markedly enhanced the degradation rate, likely due to catalyst accumulation resulting from improved MB adsorption facilitated by the larger quantity of the BC support matrix within the composite.

### 3.3. Impact of pH

The pH of the dye solution plays a crucial role in governing the adsorption behavior of the composite and, consequently, its photocatalytic degradation efficiency. To examine the effect of pH on MB removal, solutions with different pH values were adjusted using 0.1 N HCl and 0.1 N NaOH. The point of zero charge (pHpzc) of the 5CC composite was determined using the pH-drift (ΔpH) method, wherein the change in pH after equilibration ($\Delta pH = pH_f - pH_i$) was monitored. As shown in Fig. 5(b), the ΔpH plot crosses zero at pH 5.37, indicating the pHpzc of the composite. The degradation efficiency increases steadily from pH 1 to 8 and reaches a maximum at pH 8 (Fig. 5(c)). This trend reflects the increasing surface negativity and enhanced electrostatic attraction toward cationic MB molecules. The efficiency remains nearly stable from pH 8 to 10, showing minimal variation. Under strongly alkaline conditions, the possible formation of metal hydroxide species and deprotonation of MB may influence the absorbance characteristics, as supported by UV–Vis analysis.[41]

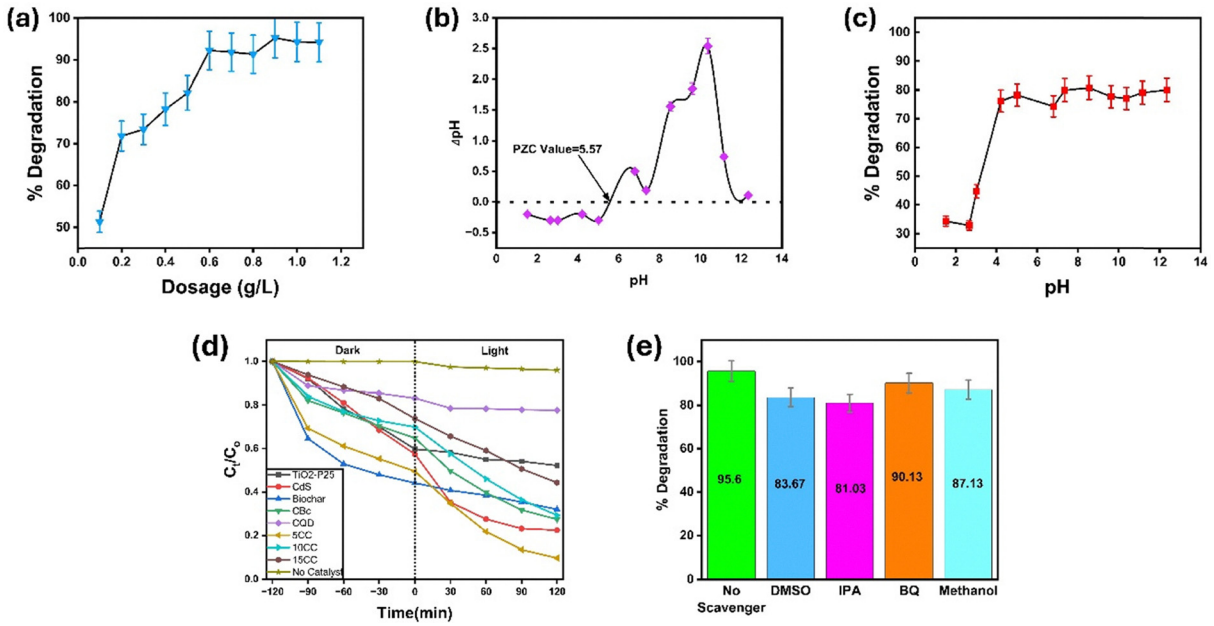


Fig. 5 (a) Influence of catalyst dosage, (b) determination of point of zero charge (PZC), (c) effect of pH on MB degradation, (d) kinetic analysis of MB degradation under visible-light irradiation, and (e) active species trapping (scavenger) studies.

### 3.4. Photocatalytic degradation kinetics

For the photocatalytic kinetic experiments, 10 mL of a 10 ppm pollutant solution was employed with 6 mg of the catalyst. Fig. 5(d) shows the limited effectiveness of photolysis alone for the removal of MB, showing only a slight 3% reduction in absorbance after 120 minutes of visible-light irradiation. This negligible change indicates the strong photostability of MB and its resistance to light-induced degradation. Under dark conditions, after 120 minutes of attaining adsorption–desorption equilibrium, the absorbance data were studied. The BC sample had the maximum adsorption with 53.129% whereas the rest of the samples, like commercially used $TiO_2$-P25, CBc, CdS,5CC,10CC,15CC and CQD had an adsorption of 36.57, 31.01, 39.02, 47.42, 25.66, 15.19 and 11.61% of adsorption. The increased porosity of BC makes the sample adsorb the dye in dark conditions than the other samples. Upon the illumination for 120 minutes after dark reactions, the absorbance of the solutions is studied using a UV-Vis spectrometer. The photocatalytic degradation by the 5CC sample was the maximum, reaching a 95.63% dye degradation, which was the maximum among the bare and other composite samples. The degradation efficiencies for the samples were of the order 5CC(95%) > CdS(76%) > 10CC(71%) > CBc(70%) > BC(66%) > 15CC(62%) > $TiO_2$-P25(45%). To further confirm the degradation process by 5CC, the temporal UV–Vis absorption spectra of MB were recorded during photocatalysis (Fig. S3, SI). A gradual decrease in the characteristic absorption peak of MB at ~658 nm was observed with increasing irradiation time, eventually leading to its near disappearance. This spectral evolution confirms the effective degradation of the dye molecules under visible-light irradiation. Furthermore, the photocatalytic degradation kinetics of MB were quantitatively evaluated by fitting the experimental data to a pseudo-first-order kinetic model (eqn (3)):

$$\ln(C_t/C_0) = -kt \quad (3)$$

In this model, $C_0$ and $C_t$ represent the initial and time-dependent concentrations of MB, respectively, while $k$ denotes the rate constant ($min^{-1}$). The linear relationship between $\ln(C_t/C_0)$ and irradiation time for various catalysts is depicted in Fig. 5(d), and the corresponding degradation rate constants are summarized in Table 2.

The synergistic interaction among CdS, BC, and CQD components was evaluated by determining the synergy factor (K), which was calculated using eqn (4):

$$K = \frac{k_{CdS+BC+CQDs}}{k_{CdS} + k_{CQDs} + k_{BC}} \quad (4)$$

where $k_{(CdS+BC+CQD)}$, $k_{CdS}$, $k_{BC}$, and $k_{CQD}$ represent the photodegradation rate constants for the ternary composite, CdS, BC, and CQD, respectively. The calculated synergy factors for 5CC, 10CC, and 15CC were 1.033, 0.542, and 0.322, respectively. Among the composites, 5CC exhibited the highest synergy factor, which correlates with its superior photocatalytic efficiency and the highest rate constant of 0.0061 $min^{-1}$.

Table 2 Rate constants and Synergy factors

| Sample | Rate constant ($min^{-1}$) | Synergy factor (K) |
|---|---|---|
| $TiO_2$ | 0.0005 | — |
| CdS | 0.0033 | — |
| BC | 0.0011 | — |
| CQD | 0.0015 | — |
| CBc | 0.0031 | 0.704 |
| 5CC | 0.0061 | 1.033 |
| 10CC | 0.0032 | 0.542 |
| 15CC | 0.0019 | 0.322 |

The enhanced performance is attributed to the synergistic interaction among the components, where CQD act as efficient electron mediators that facilitate charge separation, while biochar provides a porous structure that improves dye adsorption and promotes effective pollutant–catalyst interaction. As a result, the 5CC composite demonstrates improved photocatalytic activity compared to the individual components.

### 3.5. Influence of scavengers and plausible photocatalytic mechanism

The degradation of MB on the nanocomposite surface is governed by an integrated charge-transfer process, wherein CB electrons, VB holes, and reactive oxygen species (ROS) collectively drive the photocatalytic reaction. To determine the key reactive species participating in the photocatalytic degradation, scavenging experiments were conducted in which 1mM of isopropyl alcohol (IPA), dimethyl sulfoxide (DMSO), benzoquinone (BQ), and methanol served as quenchers for ·OH, $e^-$, $\cdot O_2^-$, and $h^+$, respectively (Fig. 5(e)).[42] Although DMSO is widely recognized as a hydroxyl-radical (•OH) scavenger, several studies have demonstrated that it can also effectively quench conduction-band electrons in semiconductor photocatalytic systems due to its strong electron-accepting ability and rapid reaction with solvated electrons. The MB degradation efficiency decreased significantly in the presence of IPA (95.6% → 81%) and DMSO (95.6% → 83.7%), suggesting that hydroxyl radicals (·OH) and electrons play a major role in the degradation pathway. Methanol reduced the degradation efficiency to 87.1%, indicating that photogenerated holes also contribute directly to oxidation processes and indirectly to ·OH generation. In contrast, BQ led to a moderate decrease (90.1%), confirming that $\cdot O_2^-$ radicals are present but act mainly as secondary oxidants. These observations clearly demonstrate that ·OH and electrons are the primary reactive species, while $h^+$ and $\cdot O_2^-$ play auxiliary roles in MB mineralization, consistent with previous scavenger-based mechanistic studies.[43]

The plausible photocatalytic degradation mechanism is illustrated in Scheme 2. Based on the band structure analysis obtained from UV–Vis DRS and Mott–Schottky measurements, the materials exhibit n-type semiconductor behavior with suitable conduction and valence band positions that thermodynamically favor the generation of reactive oxygen species such as $\cdot O_2^-$ and ·OH under visible-light irradiation. Upon visible-light excitation, CdS, CQD, and BC can absorb photons and generate electron–hole pairs.[44] The formation of the CQD/CdS/BC heterostructure facilitates efficient charge separation and rapid

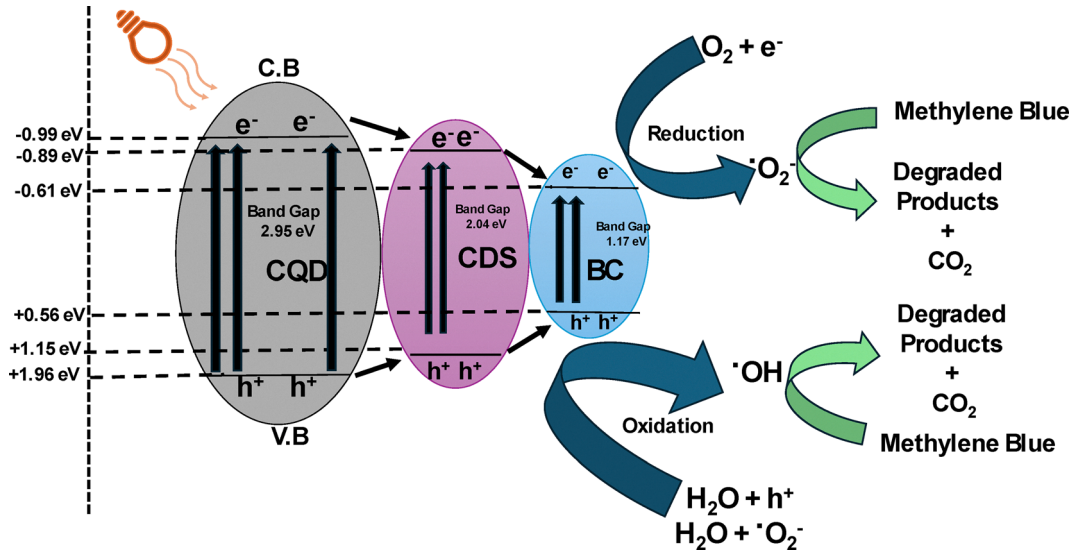


Scheme 2 Plausible photocatalytic degradation mechanism.

interfacial charge migration. The photoexcited electrons from CQD and CdS migrate through the heterojunction and are effectively transferred to the BC matrix, which acts as an electron mediator and reservoir, thereby suppressing electron–hole recombination. These accumulated electrons subsequently react with dissolved $O_2$ molecules to generate superoxide radicals ($\cdot O_2^-$). Meanwhile, the photogenerated holes from the valence bands of the semiconducting components participate in oxidation reactions, converting $H_2O$ or surface –OH groups into highly reactive hydroxyl radicals (·OH). In addition, the porous and defect-rich structure of BC enhances the adsorption of MB molecules near the active sites, increasing the contact between pollutants and reactive oxygen species. The synergistic action of ·OH (dominant), $h^+$, and $\cdot O_2^-$ radicals results in progressive degradation of MB through *N*-demethylation, chromophore cleavage, and breakdown of the aromatic framework, ultimately leading to the formation of smaller intermediates and mineralized products such as $CO_2$ and $H_2O$.

1. Photon excitation:

$$CdS + h\nu \rightarrow e^-(CB(CdS)) + h^+(VB(CdS)) \quad (5)$$

$$CQD + h\nu \rightarrow e^-(CB(CQD)) + h^+(VB(CQD)) \quad (6)$$

$$BC + h\nu \rightarrow e^-(CB(BC)) + h^+(VB(BC)) \quad (7)$$

2. Charge transfer and stabilization:

$$e^-(CB(CQD)) \rightarrow e^-(CB(CdS)) \rightarrow BC \text{ (electron mediator and sink)} \quad (8)$$

3. Superoxide radical generation:

$$O_2 + e^- \rightarrow O_2^- \quad (9)$$

4. Hydroxyl radical generation:

$$h^+ + H_2O/OH^- \rightarrow \cdot OH + H^+ \quad (10)$$

5. Direct hole oxidation of MB:

$$MB + h^+ \rightarrow \text{oxidized intermediates} \quad (11)$$

6. Final degradation/mineralization:

$$MB + (\cdot OH/\cdot O_2^-/h^+) \rightarrow \text{degraded products} \rightarrow CO_2 + H_2O \quad (12)$$

### 3.6. Proposed degradation pathway of MB over the 5CC

The possible degradation pathway of MB over the synthesized photocatalyst was proposed based on the intermediates identified from HRMS (high-resolution mass spectrometry) analysis (Fig. S4, SI). The detected intermediates in Scheme 3 indicate that the degradation primarily proceeds through C–N and C–S bond cleavage, followed by oxidation, denitrification, and desulfurization reactions. Initially, the S–Cl and C–N bonds in MB are broken, leading to the generation of smaller intermediates that undergo progressive oxidation and ring-opening under the attack of reactive oxygen species (ROS). These transformations result in the breakdown of the aromatic structure and the formation of low-molecular-weight products, which are eventually mineralized into $CO_2$, $H_2O$, $NO_3^-$, and $SO_4^{2-}$. Thus, the degradation of MB follows an oxidative pathway dominated by demethylation, deamination, and aromatic ring cleavage, confirming efficient decomposition of the dye into less toxic inorganic end-products.[45]

### 3.7. Reusability studies

The long-term durability of a photocatalyst plays a pivotal role in in its suitability for practical wastewater treatment applications. To evaluate the stability of the 5CC nanocomposite, consecutive photodegradation cycles were performed using MB. As shown in Fig. 6(a), the composite maintained a high

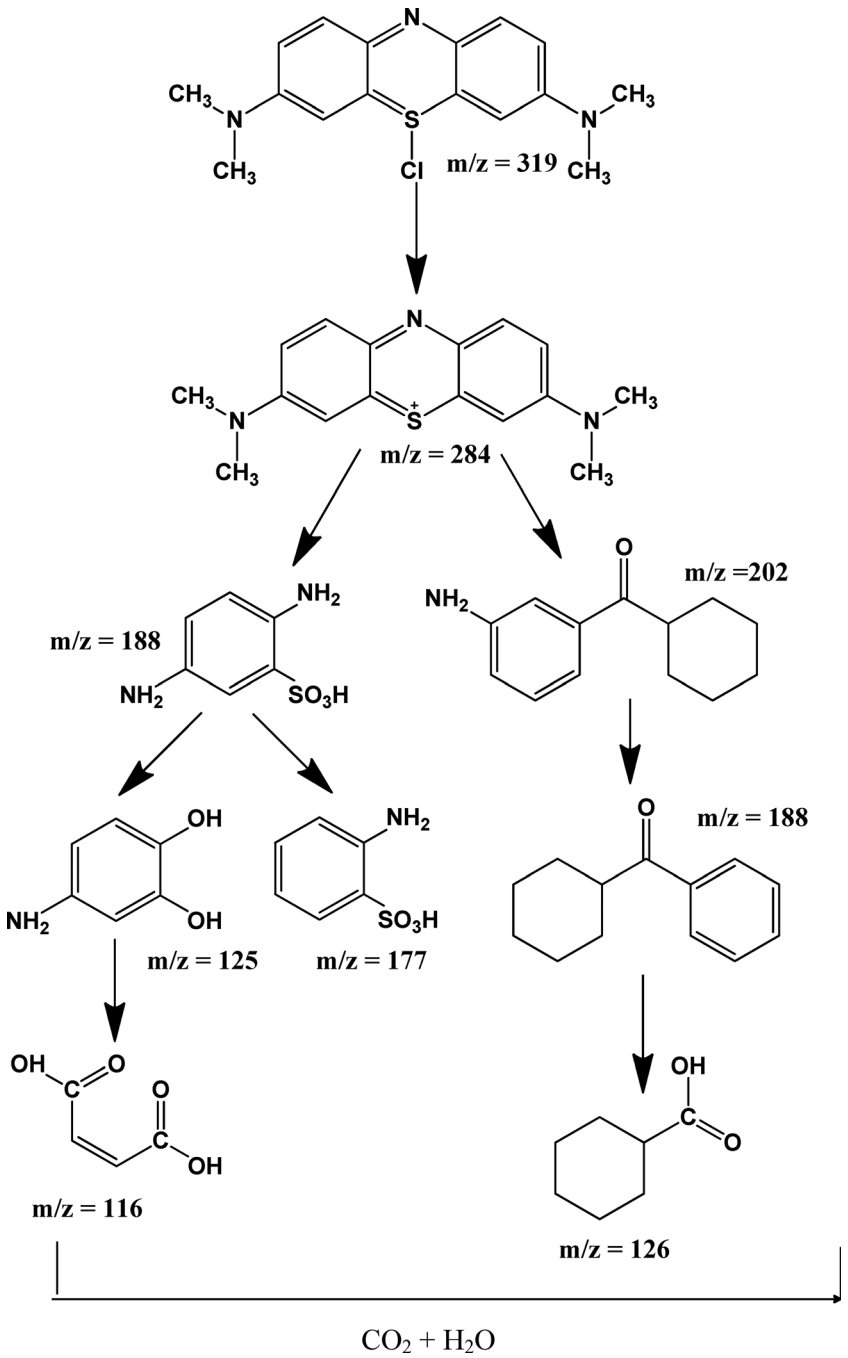


Scheme 3 Plausible degradation pathway of MB.

degradation efficiency over five successive cycles, with values of 96.2%, 95.0%, 93.7%, 91.3%, and 89.6% for the 1st, 2nd, 3rd, 4th, and 5th cycles, respectively. This gradual decrease can be attributed to the partial adsorption of dye molecules on the catalyst surface, which may slightly hinder the availability of active sites. Nevertheless, the catalyst preserved nearly 90% efficiency even after the fifth cycle, confirming its strong photostability in aqueous medium. Moreover, the reusability experiments were carried out with only 6 mg of catalyst in 10 mL of 10 ppm MB solution, demonstrating that effective degradation could be achieved at a relatively low catalyst dosage. The decomposition of organic dyes through photodegradation is evaluated by monitoring TOC (Total organic carbon) and COD (Chemical oxygen demand) levels during light exposure. After 120 minutes of visible light irradiation, reductions of 66% in TOC and 63% in COD were achieved for MB. As illustrated in Fig. 6(b), partial mineralisation was attained, while the formed intermediates exhibited minimal mineralisation potential, indicating that the organic dye was degraded into byproducts possessing lower mineralisation

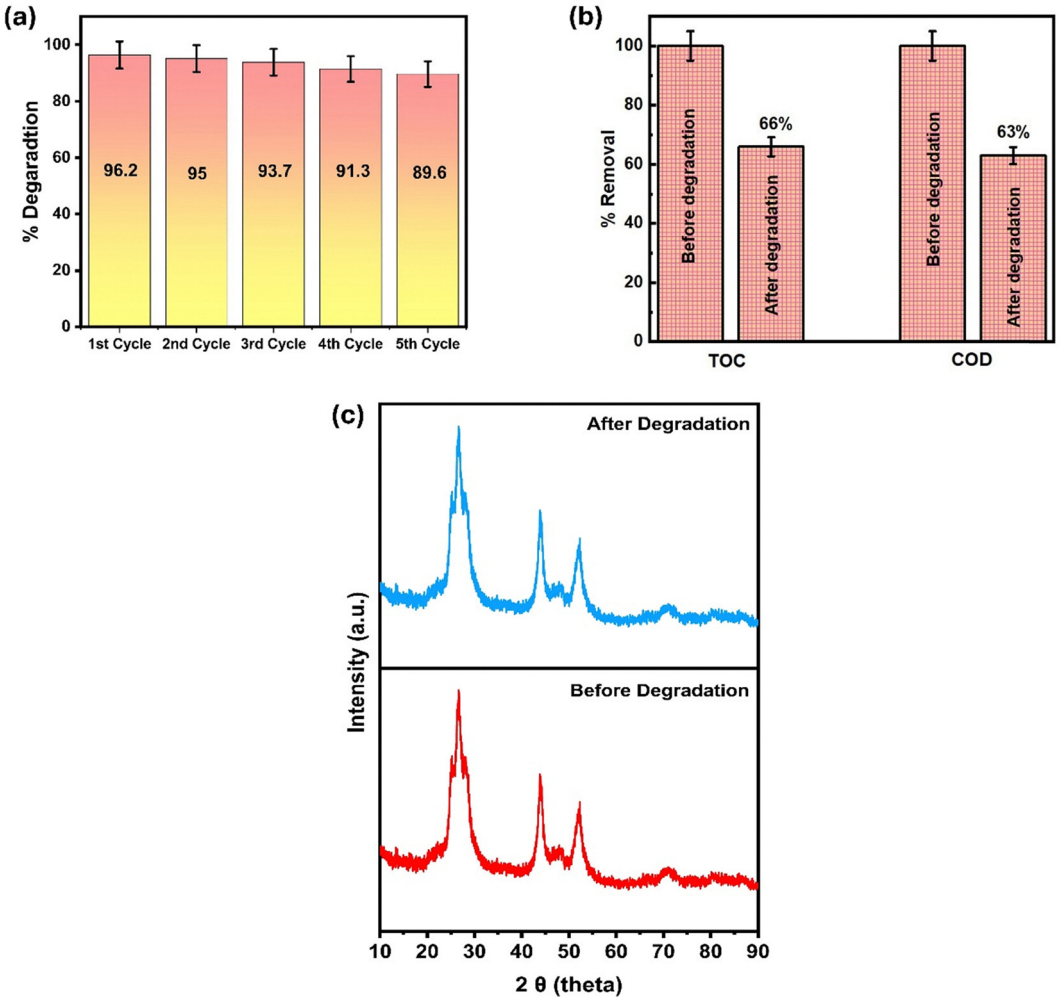


Fig. 6 (a) Cyclic stability evaluation of the photocatalyst, (b) comparison of TOC and COD values of MB solution before and after treatment, and (c) XRD profiles of 5CC obtained pre- and post-degradation.

capacity. To evaluate the potential metal leaching during the photocatalytic process, the Cd concentration in the reaction solution was analyzed using ICP–OES after the photocatalytic experiment. The detected Cd concentration was 0.0015 mg $L^{-1}$, which is lower than the permissible limit for cadmium in drinking water (0.003 mg $L^{-1}$) recommended by the World Health Organization (WHO). This result indicates minimal Cd leaching from the composite during photocatalysis. To further confirm the stability of the photocatalyst after repeated use, post-reaction XRD analysis was performed on the recovered sample (Fig. 6c). The diffraction peaks of the used 5CC closely matched those of the fresh sample, confirming the retention of the crystalline structure and indicating the absence of phase transformation or degradation of the active components after repeated photocatalytic cycles. In addition, FT-IR and FESEM analyses were carried out on the reused catalyst to further examine its structural and morphological stability. The FT-IR spectra and FESEM images (Fig. S5, SI) reveal that the characteristic functional groups and surface morphology remain largely unchanged after the reaction. These results collectively demonstrate the excellent stability of the composite and suggest that it is resistant to photocorrosion, which is a common limitation of CdS-based materials. These findings highlight that the 5CC nanocomposite not only offers excellent degradation efficiency but also combines reusability and structural integrity with reduced material consumption, making it a promising candidate for the sustainable treatment of persistent organic dyes.

### 3.8. Comparison from the literature

Table 3 presents a comparative summary of MB degradation efficiencies reported in the literature for various photocatalysts.

## 4. Conclusion

In summary, a green-synthesised CQD@CdS/biochar hybrid photocatalyst was successfully fabricated using orange peel powder as a sustainable carbon precursor and an eco-friendly aloe vera solvent system. Comprehensive structural, morphological, and optical characterizations (XRD, FTIR, XPS, FESEM, UV–Vis

Table 3 Comparison of MB degradation performance with reported photocatalysts

| Photocatalyst | Dose | Time (min) | Degradation efficiency % | Ref. |
|---|---|---|---|---|
| PVP-capped CdS NPs | 100 mg $L^{-1}$ | 360 | 81 | 46 |
| ZnS/CdS | 100 mg $L^{-1}$ | 360 | 73 | 47 |
| Zinc oxide-coated biochar (ZnO/BC) | 100 mg $L^{-1}$ | 120 | 92 | 48 |
| Cl/CQDs | 5 mL | 240 | 56 | 49 |
| ZIF-8@N-CQDs/ZIF-67 | 0.5 g $L^{-1}$ | 180 | 94 | 50 |
| CQD@CdS/Biochar | 0.6 g $L^{-1}$ | 120 | 96.2 | This work |

DRS, PL, and BET) confirmed the formation of a well-coupled ternary composite, where CQD, CdS and biochar acted synergistically to enhance light absorption, facilitate charge separation, and suppress electron–hole recombination. The optimized photocatalyst exhibited exceptional photocatalytic activity toward MB degradation, achieving a degradation efficiency of 96.2% within 120 min, with a rate constant of 0.0061 $min^{-1}$, surpassing the performance of pristine CdS and BC. The composite also demonstrated remarkable mineralisation ability, with COD and TOC reductions of 63% and 66%, respectively, confirming the efficient conversion of MB into less toxic end products. Radical trapping experiments identified $^{\bullet}OH$ as the dominant reactive species responsible for the photocatalytic process, while HRMS analysis revealed the formation of low-molecular-weight intermediates and clarified the possible degradation pathway. The photocatalyst maintained outstanding reusability and stability over 5 cycles, retaining more than 89.6% of its activity, with no significant structural changes observed after repeated use. Overall, this study demonstrates that orange-peel-derived CQD@CdS/biochar functions as an efficient, reusable, and eco-friendly photocatalyst, capable of achieving high degradation and mineralization efficiencies of organic pollutants under visible light irradiation. The synergistic interaction among CdS, CQD, and biochar offers valuable insights into designing next-generation green photocatalysts for sustainable wastewater treatment and environmental purification applications.

## Author contributions

Akash M. Nair: designed and performed the experiments, writing – original draft, Palkaran Sethi: methodology, analyzed data and cowrote the paper, Jasminder Singh: visualization, formal analysis, writing – review and editing, editing & finalization of manuscript, Soumen Basu: conceptualization, funding acquisition, editing & finalization of manuscript.

## Consent for publication

All authors approved the final manuscript and the submission to this journal.

## Conflicts of interest

The authors declare that they have no conflicting interests.

## Data availability

All data supporting the findings of this study are available within the article and its supplementary information (SI) file. Supplementary information: additional raw data, characterization files, or experimental details can be provided by the corresponding author upon reasonable request. See DOI: https://doi.org/10.1039/d6ma00043f.

## Acknowledgements

No funds, grants, or other support was received.

## References

1 B. Garg, P. Sethi and S. Basu, Strategic Innovation in CuBTC/PANI Nanocomposites for Dye Remediation: A Holistic Approach for Enhancing Adsorption, Isotherms, and Kinetic Studies, *RSC Sustainability*, 2025, **3**, 2311–2324, DOI: 10.1039/d5su00056d.

2 M. T. Yagub, T. K. Sen, S. Afroze and H. M. Ang, Dye and Its Removal from Aqueous Solution by Adsorption: A Review, *Adv. Colloid Interface Sci.*, 2014, **209**, 172–184, DOI: 10.1016/j.cis.2014.04.002.

3 G. Crini, Non-Conventional Low-Cost Adsorbents for Dye Removal: A Review, *Bioresour. Technol.*, 2006, **97**(9), 1061–1085, DOI: 10.1016/j.biortech.2005.05.001.

4 T. Robinson, G. McMullan, R. Marchant and P. Nigam, Remediation of Dyes in Textile Effluent: A Critical Review on Current Treatment Technologies with a Proposed Alternative, *Bioresour. Technol.*, 2001, **77**(3), 247–255, DOI: 10.1016/S0960-8524(00)00080-8.

5 S. Banerjee and M. C. Chattopadhyaya, Adsorption Characteristics for the Removal of a Toxic Dye, Tartrazine from Aqueous Solutions by a Low Cost Agricultural by-Product, *Arabian J. Chem.*, 2017, **10**, S1629–S1638, DOI: 10.1016/j.arabjc.2013.06.005.

6 H. Bansal, P. Sethi and S. Basu, Nanoflower-like ZnO-Carbon Quantum Dot Heterostructures for Solar-Driven Degradation of Methylene Blue: A High-Performance and Recyclable Photocatalyst for Sustainable Wastewater Treatment, *Mater. Adv*, 2025, **6**, 7585–7598, DOI: 10.1039/d5ma00804b.

7 C. Peter, D. Hongwan, A. Küpfer and B. H. Lauterburg, Pharmacokinetics and Organ Distribution of Intravenous and Oral Methylene Blue, *Eur. J. Clin. Pharmacol.*, 2000, **56**(3), 247–250, DOI: 10.1007/s002280000124.

8 P. K. Gillman, CNS Toxicity Involving Methylene Blue: The Exemplar for Understanding and Predicting Drug Interactions That Precipitate Serotonin Toxicity, *J. Psychopharmacol.*, 2010, **25**(3), 429–436, DOI: 10.1177/0269881109359098.

9 P. Sethi, S. Barman and S. Basu, CuBTC–Clay Composites with Tunable Ratios for Antibiotic Removal: Unraveling Isotherm, Kinetic, and Thermodynamic Study, *Mater. Adv.*, 2025, **6**, 6370–6385, DOI: 10.1039/D5MA00639B.

10 G. H. Shahverdizadeh, K. Seyyedi, A. Mehrizad, R. Majdan-Cegincara, S. Jamshidi, E. Ghasemi, P. Gharbani, M. Farbodi and M. Es'haghi, Recent Insights into G-$C_3N_4$ Based Composites for Methylene Blue Photocatalytic Degradation, *Results Eng.*, 2026, **29**, 108595, DOI: 10.1016/j.rineng.2025.108595.

11 P. Sethi, S. Barman and S. Basu, Strategic Tuning of GO Ratios in CuBTC-GO Nanocomposites for next-Generation Tetracycline Adsorption: A Deep Dive into Isotherms, Kinetics, and Thermodynamics, *Sep. Purif. Technol.*, 2025, **361**, 131311, DOI: 10.1016/j.seppur.2024.131311.

12 A. Ahmad, M. Rafatullah, O. Sulaiman, M. H. Ibrahim and R. Hashim, Scavenging Behaviour of Meranti Sawdust in the Removal of Methylene Blue from Aqueous Solution, *J. Hazard. Mater.*, 2009, **170**(1), 357–365, DOI: 10.1016/j.jhazmat.2009.04.087.

13 B.-B. Lee, K.-H. Choo, D. Chang and S.-J. Choi, Optimizing the Coagulant Dose to Control Membrane Fouling in Combined Coagulation/Ultrafiltration Systems for Textile Wastewater Reclamation, *Chem. Eng. J.*, 2009, **155**(1), 101–107, DOI: 10.1016/j.cej.2009.07.014.

14 N. Hilal, H. Al-Zoubi, N. A. Darwish, A. W. Mohamma and M. Abu Arabi, A Comprehensive Review of Nanofiltration Membranes:Treatment, Pretreatment, Modelling, and Atomic Force Microscopy, *Desalination*, 2004, **170**(3), 281–308, DOI: 10.1016/j.desal.2004.01.007.

15 M. K. Sinha and M. K. Purkait, Increase in Hydrophilicity of Polysulfone Membrane Using Polyethylene Glycol Methyl Ether, *J. Memb. Sci.*, 2013, **437**, 7–16, DOI: 10.1016/j.memsci.2013.03.003.

16 S. Ahmed, M. G. Rasul, W. N. Martens, R. Brown and M. A. Hashib, Heterogeneous Photocatalytic Degradation of Phenols in Wastewater: A Review on Current Status and Developments, *Desalination*, 2010, **261**(1), 3–18, DOI: 10.1016/j.desal.2010.04.062.

17 M. N. Chong, B. Jin, C. W. K. Chow and C. Saint, Recent Developments in Photocatalytic Water Treatment Technology: A Review, *Water Res.*, 2010, **44**(10), 2997–3027, DOI: 10.1016/j.watres.2010.02.039.

18 M. Es'hagi, M. Farbodi, P. Gharbani, E. Ghasemi, S. Jamshidi, R. Majdan-Cegincara, A. Mehrizad, K. Seyyedi and G. H. Shahverdizadeh, A Comparative Review on the Mitigation of Metronidazole Residues in Aqueous Media Using Various Physico-Chemical Technologies, *Anal. Methods*, 2024, **16**(43), 7294–7310, DOI: 10.1039/D4AY01502A.

19 W.-J. Ong, L.-L. Tan, Y. H. Ng, S.-T. Yong and S.-P. Chai, Graphitic Carbon Nitride (g-$C_3N_4$)-Based Photocatalysts for Artificial Photosynthesis and Environmental Remediation: Are We a Step Closer To Achieving Sustainability, *Chem. Rev.*, 2016, **116**(12), 7159–7329, DOI: 10.1021/acs.chemrev.6b00075.

20 H. Xu, L. Wu, L. Jin and K. Wu, Combination Mechanism and Enhanced Visible-Light Photocatalytic Activity and Stability of CdS/g-$C_3N_4$ Heterojunctions, *J. Mater. Sci. Technol.*, 2017, **33**(1), 30–38, DOI: 10.1016/j.jmst.2016.04.008.

21 K. Alamelu and B. M. Jaffar Ali, $TiO_2$-Pt Composite Photocatalyst for Photodegradation and Chemical Reduction of Recalcitrant Organic Pollutants, *J. Environ. Chem. Eng.*, 2018, **6**(5), 5720–5731, DOI: 10.1016/j.jece.2018.08.042.

22 C. Deng, X. Ling, L. Peng, T. Wang, R. Xu, Y. Zhu, W. Zhang, P. Sun, Y. Wu, H. Hu, Y. Han and H. Le, Constructing Nano CdS-Decorated Porous Biomass-Derived Carbon for Multi-Channel Synergetic Photocatalytic Hydrogen Evolution under Solar Lighting, *Appl. Surf. Sci.*, 2023, **623**, 157065, DOI: 10.1016/j.apsusc.2023.157065.

23 P. C. Nethravathi, M. V. Manjula, S. Devaraja, M. Sakar and D. Suresh, Eco-Friendly Preparation of $Bi_2O_3$, Ag-$Bi_2O_3$ and Ag-$Bi_2O_3$-RGO Nanomaterials and Their Photocatalytic H2 Evolution, Dye Degradation, Nitrite Sensing and Biological Applications, *J. Photochem. Photobiol., A*, 2023, **435**, 114295, DOI: 10.1016/j.jphotochem.2022.114295.

24 M. Kheirabadi, M. Samadi, E. Asadian, Y. Zhou, C. Dong, J. Zhang and A. Z. Moshfegh, Well-Designed Ag/ZnO/3D Graphene Structure for Dye Removal: Adsorption, Photocatalysis and Physical Separation Capabilities, *J. Colloid Interface Sci.*, 2019, **537**, 66–78, DOI: 10.1016/j.jcis.2018.10.102.

25 K. R. Deepak, S. Mohan, P. Dinesha and R. Balasubramanian, $CO_2$ Uptake by Activated Hydrochar Derived from Orange Peel (Citrus Reticulata): Influence of Carbonization Temperature, *J. Environ. Manage.*, 2023, **342**, 118350, DOI: 10.1016/j.jenvman.2023.118350.

26 L. Han, Y. Guo, H. Zhang, Z. Wang, F. Zhang, Y. Wang, X. Li, Y. Wang and J. Ye, Preparation of Carbon Quantum Dot Fluorescent Probe from Waste Fruit Peel and Its Use for the Detection of Dopamine, *RSC Adv.*, 2024, **14**(3), 1813–1821, DOI: 10.1039/d3ra06799h.

27 A. M. Nair, A. Mehta, M. Singh, S. Basu and J. Singh, Green Synthesis of Ni/Mn-Doped CdS Nanoparticles Using Aloe Vera Extract for Rhodamine B Degradation Under Visible Light, *Top. Catal.*, 2025, 1–15, DOI: 10.1007/s11244-025-02205-w.

28 S. Shen, L. Yan, K. Song, Z. Lin, Z. Wang, D. Du and H. Zhang, $NiSe_2$/CdS Composite Nanoflakes Photocatalyst with Enhanced Activity under Visible Light, *RSC Adv.*, 2020, **10**(69), 42008–42013, DOI: 10.1039/d0ra09272j.

29 A. K. Kercher and D. C. Nagle, Microstructural Evolution during Charcoal Carbonization by X-Ray Diffraction Analysis, *Carbon*, 2003, **41**(1), 15–27, DOI: 10.1016/S0008-6223(02)00261-0.

30 K. Ali, P. Sethi and S. Basu, ZIF-67/CQD Nanohybrids for Combined Adsorptive and Photocatalytic Removal of Tetracycline: Kinetic, Isotherm, and Mechanistic Insights, *RSC Sustainability*, 2026, **4**, 1436–1455, DOI: 10.1039/D5SU00898K.

31 S. Rajeshkumar, C. Malarkodi, K. Paulkumar, M. Vanaja, G. Gnanajobitha and G. Annadurai, Algae Mediated Green Fabrication of Silver Nanoparticles and Examination of Its Antifungal Activity against Clinical Pathogens, *Int. J. Met.*, 2014, **2014**(1), 692643, DOI: 10.1155/2014/692643.

32 A. Lateef, M. A. Azeez, T. B. Asafa, T. A. Yekeen, A. Akinboro, I. C. Oladipo, L. Azeez, S. E. Ajibade, S. A. Ojo, E. B. Gueguim-Kana and L. S. Beukes, Biogenic Synthesis of Silver Nanoparticles Using a Pod Extract of Cola Nitida: Antibacterial and Antioxidant Activities and Application as a

Paint Additive, *J. Taibah Univ. Sci.*, 2016, **10**(4), 551–562, DOI: 10.1016/j.jtusci.2015.10.010.

33 X. Zhu, Y. Zeng, X. Zhao, D. Liu, W. Lei and S. Lu, Biomass-Derived Carbon and Their Composites for Supercapacitor Applications: Sources, Functions, and Mechanisms, *Eco-Energy*, 2025, **3**(3), e70000, DOI: 10.1002/ece2.70000.

34 K. Hola, Y. Zhang, Y. Wang, E. P. Giannelis, R. Zboril and A. L. Rogach, Carbon Dots—Emerging Light Emitters for Bioimaging, Cancer Therapy and Optoelectronics, *Nano Today*, 2014, **9**(5), 590–603, DOI: 10.1016/j.nantod.2014.09.004.

35 J. Hou, Q. Dou, T. Jiang, J. Yin, J. Liu, Y. Li, G. Zhang and X. Wang, BiOCl/Cattail Carbon Composites with Hierarchical Structure for Enhanced Photocatalytic Activity, *Sol. Energy*, 2020, **211**, 1263–1269, DOI: 10.1016/j.solener.2020.10.051.

36 U. Winkler, D. Eich, Z. H. Chen, R. Fink, S. K. Kulkarni and E. Umbach, Detailed Investigation of CdS Nanoparticle Surfaces by High-Resolution Photoelectron Spectroscopy, *Chem. Phys. Lett.*, 1999, **306**(1), 95–102, DOI: 10.1016/S0009-2614(99)00427-3.

37 F. A. Ganaie, Z. ul-Haq, A. Bashir, A. Qureashi, I. Nazir, K. Fatima, A. H. Pandith and M. A. Bhat, SnS2 Decorated Biochar: A Robust Platform for the Photocatalytic Degradation and Electrochemical Sensing of Pollutants, *New J. Chem.*, 2024, **48**(16), 7111–7124, DOI: 10.1039/d4nj00231h.

38 L. Zhang, C. Zhang, J. Li, K. Sun, J. Zhang, M. Huang and J. Wang, Hydrothermally Prepared Unactivated Bean Sprouts Biochar Supported CdS with Significantly Enhanced Photocatalytic Hydrogen Evolution Activity, *Catal. Commun.*, 2024, **187**, 106861, DOI: 10.1016/j.catcom.2024.106861.

39 P. Sethi, S. Basu and S. Barman, Innovative CuBTC/g-$C_3N_4$ Materials for Tetracycline Mitigation: Adsorption, Photocatalysis, and Mechanistic Perspectives, *New J. Chem.*, 2025, **49**, 8454–8471, DOI: 10.1039/d5nj00556f.

40 P. Sethi, S. Barman and S. Basu, Eco-Friendly Tetracycline Remediation Using Robust and Highly Reusable ZIF-67/g-$C_3N_4$ Nanocomposites with Coupled Adsorption and Photocatalytic Pathways: A Deep Dive into Isotherms, Kinetics, Thermodynamics, and Degradation Pathways, *ACS Sustainable Resour. Manage.*, 2025, **3**, 244–259, DOI: 10.1021/acssusresmgt.5c00536.

41 F. Azeez, E. Al-Hetlani, M. Arafa, Y. Abdelmonem, A. A. Nazeer, M. O. Amin and M. Madkour, The Effect of Surface Charge on Photocatalytic Degradation of Methylene Blue Dye Using Chargeable Titania Nanoparticles, *Sci. Rep.*, 2018, **8**(1), 7104, DOI: 10.1038/s41598-018-25673-5.

42 A. Kundu, S. Sharma and S. Basu, Modulated BiOCl Nanoplates with Porous G-$C_3N_4$ Nanosheets for Photocatalytic Degradation of Color/Colorless Pollutants in Natural Sunlight, *J. Phys. Chem. Solids*, 2021, **154**, 110064, DOI: 10.1016/j.jpcs.2021.110064.

43 T. T. D. Nguyen, D. Nguyen, P. P. Vo, H. N. Doan, H. T. N. Pham, V. H. Hoang, K. Tien Le, K. Kinashi, V. T. Huynh and P. T. Nguyen, The Roles of Ethanol and Isopropanol as Hole Scavengers in the Photoreduction Reaction of Graphene Oxide by $TiO_2$: A Competition of Oxygenated Groups Removal and Carbon Defects Invasion, *J. Mol. Liq.*, 2023, **381**, 121831, DOI: 10.1016/j.molliq.2023.121831.

44 J.-X. Li, R.-L. Zhang, Z.-J. Pan, Y. Liao, C.-B. Xiong, M.-L. Chen, R. Huang, X.-H. Pan and Z. Chen, Preparation of CdS@C Photocatalyst Using Phytoaccumulation Cd Recycled From Contaminated Wastewater, *Front. Chem.*, 2021, **9**, 717210.

45 S. Wang and Y. Zhang, Degradation of Methylene Blue by an E-Fenton Process Coupled with Peroxymonosulfate via Free Radical and Non-Radical Oxidation Pathways, *New J. Chem.*, 2023, **47**(7), 3616–3627, DOI: 10.1039/d2nj05504j.

46 N. Soltani, E. Saion, W. Mahmood Mat Yunus, M. Navasery, G. Bahmanrokh, M. Erfani, M. R. Zare and E. Gharibshahi, Photocatalytic Degradation of Methylene Blue under Visible Light Using PVP-Capped ZnS and CdS Nanoparticles, *Sol. Energy*, 2013, **97**, 147–154, DOI: 10.1016/j.solener.2013.08.023.

47 N. Soltani, E. Saion, M. Z. Hussein, M. Erfani, A. Abedini, G. Bahmanrokh, M. Navasery and P. Vaziri, Visible Light-Induced Degradation of Methylene Blue in the Presence of Photocatalytic ZnS and CdS Nanoparticles, *Int. J. Mol. Sci.*, 2012, **13**(10), 12242–12258, DOI: 10.3390/ijms131012242.

48 P. Eswaran, P. D. Madasamy, K. Pillay and H. Brink, Sunlight-Driven Photocatalytic Degradation of Methylene Blue Using ZnO/Biochar Nanocomposite Derived from Banana Peels, *Biomass Convers. Biorefin.*, 2025, **15**(8), 12347–12367, DOI: 10.1007/s13399-024-05999-z.

49 Y. Cheng, M. Bai, J. Su, C. Fang, H. Li, J. Chen and J. Jiao, Synthesis of Fluorescent Carbon Quantum Dots from Aqua Mesophase Pitch and Their Photocatalytic Degradation Activity of Organic Dyes, *J. Mater. Sci. Technol.*, 2019, **35**(8), 1515–1522, DOI: 10.1016/j.jmst.2019.03.039.

50 E. S. Elmorsy, W. A. Amer, A. Mahrous and M. M. Ayad, Insight into the Novel ZIF-8@N-CQDs/ZIF-67 Nanocomposite for Photocatalytic Degradation of Methylene Blue under Visible Light Irradiation, *Mater. Sci. Eng. B*, 2023, **298**, 116900, DOI: 10.1016/j.mseb.2023.116900.